ADVANCED FUNCTIONAL MATERIALS
www.afm-journal.de

In Situ Liquid-Cell TEM Observation of Multiphase Classical and Nonclassical Nucleation of Calcium Oxalate

David J. Banner, Emre Firlar, Pavel Rehak, Abhijit H. Phakatkar, Tara Foroozan, Jodi K. Osborn, Lioudmila V. Sorokina, Surya Narayanan, Talia Tahseen, Yusuf Baggia, Petr Král, Tolou Shokuhfar,* and Reza Shahbazian-Yassar**

Calcium oxalate (CaOx) is the major phase in kidney stones and the primary calcium storage medium in plants. CaOx can form crystals with different lattice types, water contents, and crystal structures. However, the conditions and mechanisms leading to nucleation of particular CaOx crystals are unclear. Here, liquid-cell transmission electron microscopy and atomistic molecular dynamics simulations are used to study in situ CaOx nucleation at different conditions. The observations reveal that rhombohedral CaOx monohydrate (COM) can nucleate via a classical pathway, while square COM can nucleate via a non-classical multiphase pathway. Citrate, a kidney stone inhibitor, increases the solubility of calcium by forming calcium-citrate complexes and blocks oxalate ions from approaching calcium. The presence of multiple hydrated ionic species draws additional water molecules into nucleating CaOx dihydrate crystals. These findings reveal that by controlling the nucleation pathways one can determine the macroscale crystal structure, hydration state, and morphology of CaOx.

1. Introduction

Calcium oxalate ($CaC_2O_4 \cdot H_2O$, or CaOx) is an important crystal positively affecting plants and fungi, which may be involved in environmental CO_2 capture.[1–3] Oxalate sequesters calcium within sub-cellular vacuoles to regulate calcium and in effect stores excess CO_2 in plants, since oxalate is a downstream metabolite of CO_2.[1–3] This oxalate-mediated calcium storage is essential to ensure that adequate calcium is available for critical metabolic processes without causing excess free-calcium toxicity.[4–7] CaOx also provides structural support to plants.[4–7] Bacteria and some fungi are capable of catabolizing oxalate and release the stored energy via metabolic catabolism, such as the glyoxylate pathway.[8] CaOx from plants and fungi may be deposited into soil, where it stores ecological calcium.[9] As a biomineral, the presence of oxalates has been hypothesized to be indicative of non-terrestrial life in astrobiology.[10–12] In human and animal life, however, CaOx is pathogenic. CaOx is the major phase in 80% of kidney stones.[13–16] Thus, understanding the formation, crystallization, and dissolution of CaOx is essential to the biomedical field, plant biology, soil science, microbiology, and perhaps the search for extraterrestrial life.

In nature, CaOx primarily exists as CaOx monohydrate (COM), but it may also be dihydrate (COD), trihydrate (COT), or rarely amorphous (ACO), where the thermodynamic stability of COM is the highest and ACO the lowest.[17] COM is the most common CaOx phase in kidney stones, while COD is less common, and COT is exceedingly rare.[18,19] Plants primarily contain COM and COD.[5] ACO is highly unstable and quickly crystallizes environmentally, but it has been prepared in the laboratory setting by chemical stabilization of CaOx.[20–22] Many studies have characterized the

Dr. D. J. Banner
Department of Medicine
University of Illinois at Chicago
1853 W Polk St, Chicago, IL 60612, USA
Dr. D. J. Banner, Dr. E. Firlar, A. H. Phakatkar, J. K. Osborn, Dr. S. Narayana, T. Tahseen, Y. Baggia, Prof. T. Shokuhfar
Department of Bioengineering
University of Illinois at Chicago
851 Morgan St, Chicago, IL 60607, USA
E-mail: tolou@uic.edu
Dr. E. Firlar, Dr. T. Foroozan, Prof. R. Shahbazian-Yassar
Department of Mechanical and Industrial Engineering
University of Illinois at Chicago
842 West Taylor St, Chicago, IL 60607, USA
E-mail: rsyassar@uic.edu
The ORCID identification number(s) for the author(s) of this article can be found under https://doi.org/10.1002/adfm.202007736.
Dr. E. Firlar
Institute for Quantitative Biomedicine
Rutgers University
174 Frelinghuysen Rd, Piscataway, NJ 08854, USA
Dr. P. Rehak, Prof. P. Král
Department of Chemistry
University of Illinois at Chicago
845 West Taylor St, Chicago, IL 60607, USA
E-mail: pkral@uic.edu
L. V. Sorokina
Department of Civil and Materials Engineering
University of Illinois at Chicago
842 West Taylor Street, Chicago, IL 60607, USA
Prof. P. Král
Departments of Physics
Pharmaceutical Sciences and Chemical Engineering
University of Illinois at Chicago
845 West Taylor Street, Chicago, IL 60607, USA

DOI: 10.1002/adfm.202007736

© 2021 Wiley-VCH GmbH

structure, morphology, and chemical content of CaOx minerals in plants,[5] humans,[11] and in vitro chemical studies.[23–25] Transmission electron microscopy (TEM) studies of CaOx have primarily focused on ex situ interactions of CaOx with biological species or CaOx crystals formed within biological tissues,[26,27] such as renal epithelial cells,[28] or as a characterization technique for benchtop experiments.[29,30] However, no studies documented real-time CaOx nucleation.

The importance of understanding real-time nanoscale nucleation processes of CaOx is indicated by the dependence of the crystal structure and morphology of other calcium salts on their nanoscale mineralization processes.[31] The formed crystal structures and particle morphologies of CaOx also have direct effects on human health: COM binds cell walls with more strength than COD or COT.[32] Thus, previous works have hypothesized that forming COD or COT may reduce the incidence of CaOx kidney stones.[32] COM kidney stones are also more difficult for clinicians to treat. Understanding the nucleation pathways of CaOx will thus allow direct insight into the mechanisms by which CaOx forms pathogenic crystal structures. Comparison of the nucleation pathways in the presence of molecular modifiers would provide mechanistic insight into CaOx kidney stone prevention. This understanding and insight into kidney stones would benefit the health of ≈8% of the population of the USA who are personally affected by kidney stones.[33] Nationwide, current treatments costs have an annual financial burden of approximately five billion USD.[34] The associated renal damage also contributes to other major diseases, such as chronic kidney disease and heart disease.[34]

Molecular modifiers such as citrate can affect the CaOx nucleation by increasing its solubility and by other mechanisms,[35] such as altering the crystallization and facet-growth of CaOx.[36] In the Cabrera–Vermilyea (C–V) model, citrate molecules bind to the surface of a crystal growing via edge growth, and inhibits or alters the continued addition of monomers, oligomers, or polymers in the affected plane.[37,38] Alternatively, citrate may bind to the surface of the crystal and induce lattice strain.[38] This lattice strain leads to removal of ions and dissolution of the crystal at concentrations otherwise suitable for the formation of CaOx.[38] Stress in nucleating crystals induced by molecular modifiers may also directly induce their morphological changes.[39] In contrast, citrate prevented crystallization of amorphous precursors by coating the surface of the precursors, which resulted in the formation of COT rather than COM.[29]

The nucleation of CaOx crystals can be affected by many parameters. The free energy of the solution, the interfacial energy between the nucleating particles, precursors, and the solution, as well as the local saturation of the ionic species may all influence the crystal formation pathways.[40] If the free energies of different pathways are similar, multiple formation pathways may occur within the same solution.[40] CaOx may form multiple particle morphologies from the same crystal structures. For example, COM with the same monoclinic crystal structure may form rhomboid shaped pinacoids with a dominant [100] facet, rhomboid shape pinacoids with a dominant [010] facet, styloids, twins, dendrites, or agglomerates of COM crystals.[1,41,42] Factors such as pH, temperature, stirring speed, and molar concentrations have been correlated with distinct crystal morphologies.[42]

In principle, depending on the crystal formed and the crystallization conditions, the nucleation of crystals may occur through several different pathways.[43] Crystal nucleation may occur through classical crystal nucleation, where monomer units attach one after another to form a central crystalline core.[43] Alternatively, crystal nucleation may occur through formation of oligomeric or polymeric complexes, rather than individual monomers.[44] Crystal nucleation may also occur through the formation of dense liquid droplets, wherein ions aggregate together within a liquid to form an area of high ion density (spinodal separation).[45] Upon reaching a sufficiently high local concentration, the dense liquid droplet can change its composition and start to aggregate into an amorphous and (later) crystalline nucleus.[46,47] Crystallization may also occur through nucleation and oriented attachment, in which nanocrystalline precursors or amorphous precursors form and then aggregate to form a larger crystal.[40] Monomer, oligomer, or polymer nanocrystals or amorphous particles form separately.[48] These particles then orient and attach to form a larger crystal, which may involve internal reorganization of the nanocrystals.[40]

Previously, in situ atomic force microscopy (AFM) was used to study the real-time growth of CaOx from seed crystals.[36,49–53] While AFM allows analysis of material surfaces, it is unable to determine the crystal structure and local chemical changes during nucleation and growth. Graphene liquid cell (GLC) encapsulation of a liquid sample has been used for in situ imaging of colloid nanocrystals, ferritin, or bacteria.[54–57] Here, GLC within a TEM was utilized to observe real-time CaOx nucleation and mineral growth. In the experiments, a supersaturated liquid solution of calcium and oxalate ($C_2O_4H_2^{2-}$) ions was encapsulated in GLC, allowing observation of nucleation and growth of CaOx.[55,57–61] In a similar way, the effect of citrate on the mineralization of CaOx was also studied in GLC. Select-area electron diffraction (SAED) was used to characterize the crystal structure of particles formed in the GLC. Molecular dynamics (MD) simulations of CaOx formation were performed in both the absence and presence of citrate. The end-stage products of GLC TEM studies were validated by ex situ benchtop studies. The ex situ products were visualized by a scanning electron microscopy (SEM), structurally analyzed via X-ray diffraction (XRD), and chemically analyzed by electron energy loss spectroscopy (EELS) and energy dispersive X-ray spectroscopy (EDS) within scanning TEM (STEM).

2. Results

2.1. In Situ TEM Studies of CaOx Formation: Classical Nucleation

Figure 1 (Video S1, Supporting Information) shows the observed nucleation of CaOx crystal in a supersaturated solution (**Table 1**) within a GLC. The CaOx crystal nucleus grew sequentially on specific facets, as indicated by red arrows in Figure 1 (Figure S1, and Video S1, Supporting Information). Corners with an angle of 120° formed within 1 s, indicating the initial formation of a rhombohedral CaOx particle.[1,62] The morphology of the rhombohedral particle formed in Figure 1 agrees with previous reports of COM,[1] since COM is reported

© 2021 Wiley-VCH GmbH

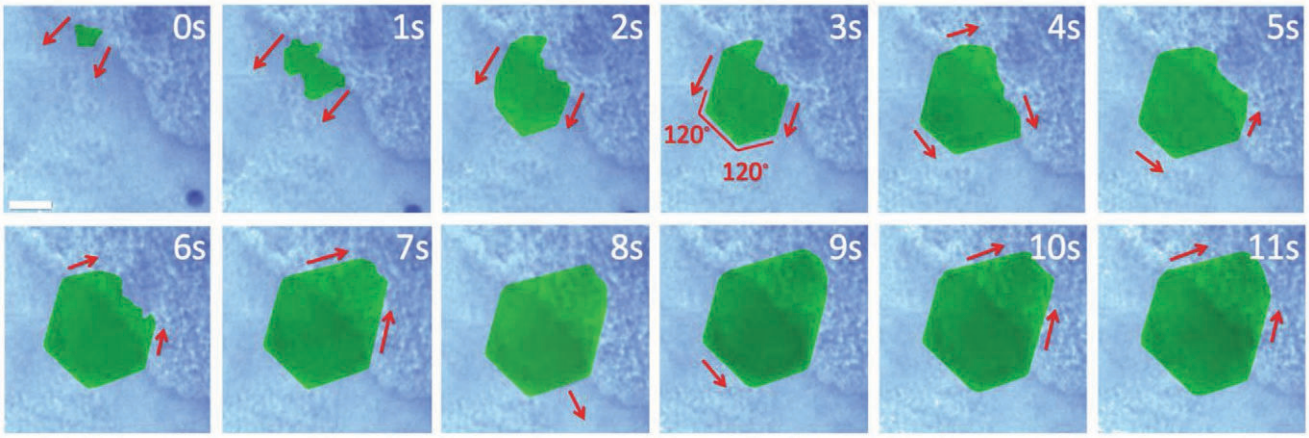


Figure 1. The classical nucleation of CaOx crystal within GLC-TEM. The process starts by the formation of a stable nucleus, followed by monomer addition to the growing crystal. The particle (green) grows along specific facets as indicated by the red arrows. The time series from the beginning of particle formation is included in the upper right corner of each image. All images were collected from the same magnification. The scale bar is 50 nm. False coloring used.

as the most stable crystal structure of CaOx, with the lowest free energy.[17] However, the particle growth in the (100) plane is not directly visible, since it is orthogonal to the image plane.

Throughout Video S1, Supporting Information, there are variations observed in the contrast of the particle. These changes in the particle contrast have been plotted in Figure S2, Supporting Information. Changes in contrast in TEM are typically the result of Rutherford scattering, which is dependent on the mass thickness contrast (Φ), and diffraction contrast. Rutherford scattering has been described as:

$$\Phi = \frac{N_0 Q_{\text{atom}} \rho \Delta D}{A} \tag{1}$$

where N_0 is Avogadro's number, the cross section of scattering is Q, ρ is density, the thickness is represented by ΔD, and A is the atomic weight.[55] Diffraction contrast may also alter the contrast of the video as described by Bragg's law. This diffraction may be described by Bragg's law

$$n\lambda = 2d\sin(\theta) \tag{2}$$

While changes such as the material density may alter the contrast, the crystalline nature of the particle in Figure 1 suggests that the density of the particle does not significantly vary.[55] Although the particle appears to be in constant orientation throughout the video, minor changes in the crystal orientation may produce minor fluctuations observed throughout Video S1, Supporting Information.[63] However, there is a significant increase in the contrast between the beginning and end of the video. This suggests that the markedly increased contrast at the end of the video compared to the beginning of the video is likely to be due to the growth in the (100) plane.[63]

In Figure 1, the particle first begins growth to the upper right of a boundary at 0 s. This boundary may represent changes in the liquid thickness. The particle may nucleate homogenously or heterogeneously. Similar particle dynamics were observed in other samples where no visible boundary is present (Figure S3, Videos S2 and S3, Supporting Information). Other particles within Video S1, Supporting Information, may be CaOx, but the lack of particle morphology prevents identification of the materials. While electron diffraction might identify the crystal structure, focusing the electron beam on beam sensitive particles may damage the particles. Diffraction of a larger area would detect the crystal shown in Figure 1, which would not provide additional information into the crystal structure of the particles.[64] However, Visual MINTEQ simulations suggest that only CaOx precipitates in the solution (Note S1, Supporting Information). The particles may be amorphous CaOx or polycrystalline CaOx, since they were not observed to form stable particle structures. Figure 1 thus appears to reveal a classical nucleation of COM, where ions, atoms, or molecular species nucleate to form a crystalline core.[43] This is followed by the attachment of individual molecular species or small oligomeric species not directly visible in TEM to the surface of the forming crystal (Video S1, Supporting Information).

Table 1. A summary of the saturation states of the CaOx solutions.

	Initial saturation index without citrate	Initial saturation index with citrate	Equilibrium saturation index without citrate	Equilibrium saturation index with citrate
COM	4.4	4	0	0
COD	4.0	3.5	−0.4	−0.4
COT	4.0	3.5	−0.4	−0.4

2.2. In Situ TEM Studies of CaOx Formation: Non-Classical Nucleation

Figure 2 (Video S4, Supporting Information) illustrates a different type of nucleation of CaOx obtained through four distinct stages. First, CaOx forms an imperfect rhombohedral precursor as indicated by 120° corners visible at 6 s (Figure 2, Figure S3, and Video S4, Supporting Information).[1,62] The particle corners are not as sharp and as clearly indicative of an ideal rhombohedral crystal as the particle in Figure 1. The particle

© 2021 Wiley-VCH GmbH

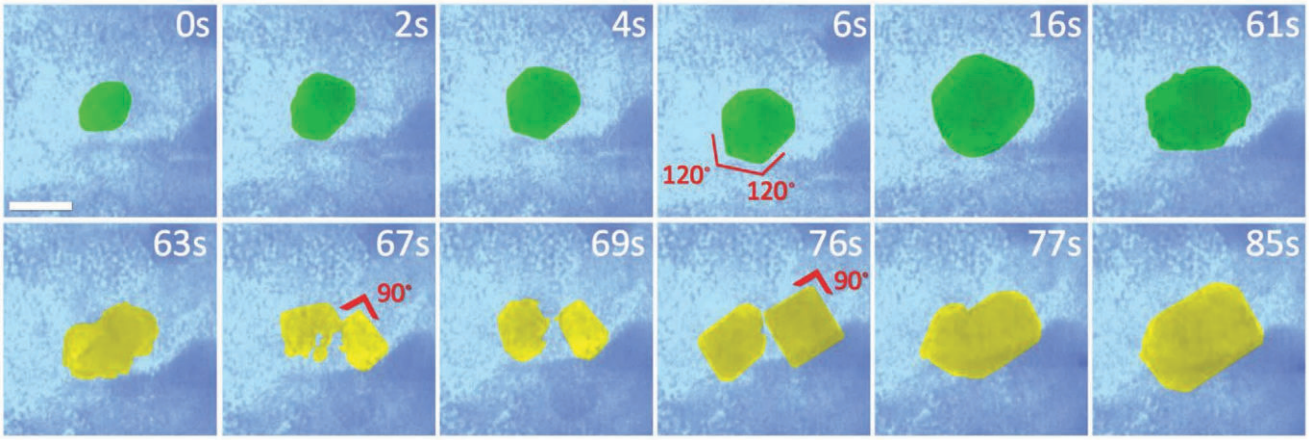


Figure 2. The non-classical formation pathway of CaOx within GLC in the absence of citrate. The particle shows initial classical formation via formation of a central nanoscale nucleus followed by ionic addition to the growing crystal from 0 to 16 s. However, throughout the video the 120° corners are not as sharp as in Figure 1 (Figure S1 and Video S1, Supporting Information), indicating the particle is not fully crystalline. Eventually, the sharpness of the corners decreases at 61 s until the particles nearly, but not entirely, dissolve (63 s). The particle leaves behind two apparently amorphous particles, which then begin displaying 90° corners (67 s). The particle corners continue to sharpen throughout growth, until the two particles coalescence. The scale bar is 50 nm. False coloring used.

grows from 0 to 16 s (Figure 2, Figure S3, and Video S4, Supporting Information). Unlike Figure 1, the particle in Figure 2 partially dissolves from 16 to 69 s (Figure 2, Figure S3, and Video S4, Supporting Information). Both Figures 1 and 2 were collected from the same GLC at the same electron dose. Previous works have observed either beam induced growth or beam induced etching, but cyclic growth and dissolution was only achieved by manually increasing and decreasing the electron dose rate (Note S2, Supporting Information).[65] This suggests that the growth and subsequent dissolution of the CaOx particle in Figure 2 is not an artifact of the electron beam since the electron beam dose rate was constant.

Several alternative explanations may address the partial dissolution of the crystal observed in Figure 2. In general, nucleation and crystallization is driven by the reduction in free energy. When the chemical component is more stable as a solid crystal, a crystal forms rather than dissolved in a solution. However, the formation of the crystal is energetically costly due to the interfacial energy between the ordered crystal surface and the disordered solution.[66] The dissolution of the crystal could be due to an increase in the volumetric energy, which is no longer greater than the interfacial energy cost. This increase in volumetric energy could be due to a number of phenomena, including: 1) imperfections in the crystal structure, 2) impurities in the crystal, such as sodium or chloride contaminants, or 3) excess water in the crystal.[36,67]

Defects in the free energy of the crystal may be modeled by the following equation:

$$G = G^* + N_D \Delta H_D - T N_D \Delta S_v - T \Delta S_c (N_D) \quad (3)$$

Here, G is the Gibbs free energy, G^* is the Gibbs free energy of the perfect crystal, T is the temperature, N_D is the number of defects, ΔH_D is the enthalpy change due to the defect, S_v is the vibrational entropy due to the defect, and $\Delta S_c(N_D)$ is the change in the configurational energy.[68] This suggests that the presence of defects or additional phases within the crystal would be energetically unfavorable. Thus, in the second stage, the particle partially dissolves in Figure 2 from 16 to 69 s through an amorphous stage to relieve this high energy state (Figure 2, Figure S3, and Video S4, Supporting Information). This process may include reorganization of the crystal structure or expulsion of contaminants or water which are not visible in the GLC image.

In a third stage, the partially dissolved particles form 90° corners at 67 s (Figure 2, Figure S3, and Video S4, Supporting Information) indicative of rectangular COM, as reported in literature, rather than fully dissolving (Figure 2, Figure S3, and Video S4, Supporting Information).[1] SEM of ex situ particles also showed the formation of rectangular and rhombohedral COM (Figure S4, Supporting Information). XRD confirmed the crystal structures of ex situ samples (Figure S4, Supporting Information). The removal of the crystal imperfections, contaminants, or excess water reduces the volumetric energy and allows the growth of particles, as shown in Figure 2 from 69 to 76 s (Figure 2, Figure S3, and Video S4, Supporting Information). Finally, in a fourth stage, the particles in Figure 2 (Figure S3 and Video S4, Supporting Information) coalesce from 67 to 85 s to minimize their interfacial energy between the surface and the solution by reducing the surface area (Figure 2, Figure S3, and Video S4, Supporting Information).[69] The rectangular particles in Figure 2 may also be rhombohedral COM observed along the (111) facet. This would however require the particle to be perfectly oriented in the (111) orientation relative to the z-axis of the 2D image throughout the dynamic video. Further, no increase in contrast at the center of the particle is visible as would be expected from a rhombohedral particle observed along the (111) facet. The crystallization from an amorphous phase was confirmed via Fast Fourier Transform analysis of HR-TEM of a CaOx nanoparticle at different time steps in GLC (Figure S5 and Video S5, Supporting Information).

© 2021 Wiley-VCH GmbH

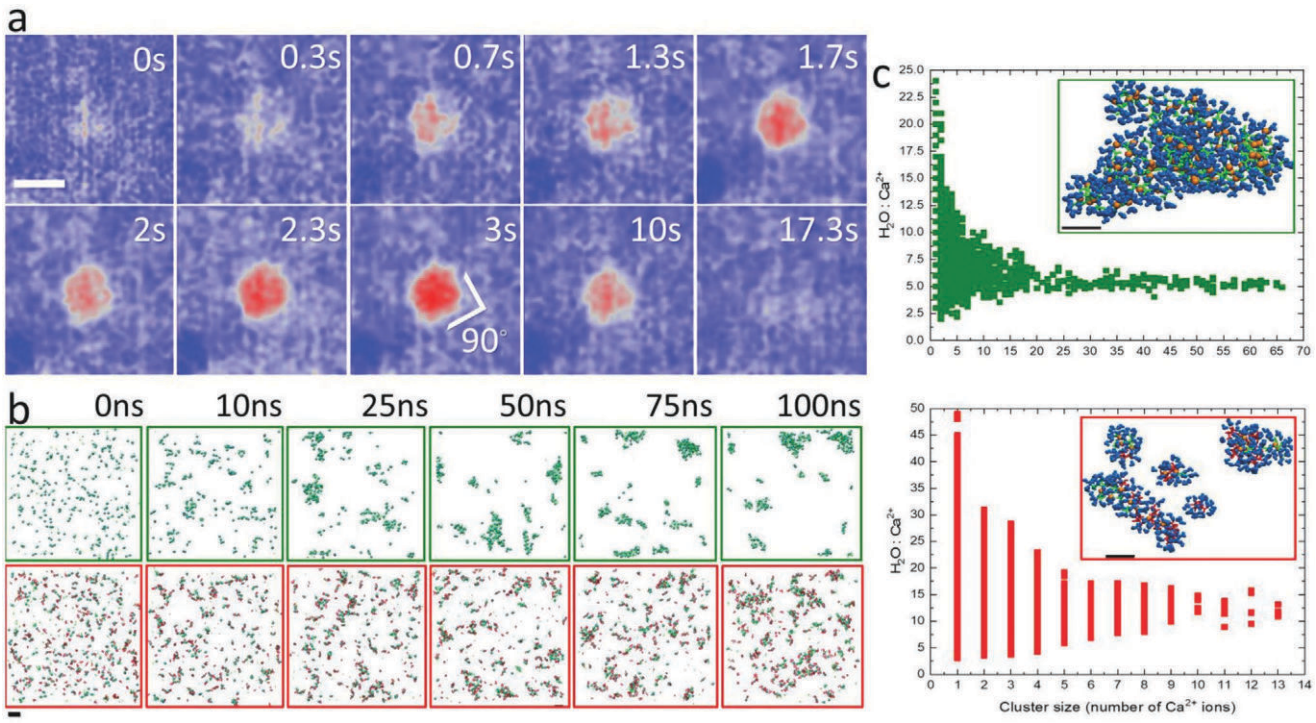


Figure 3. Repeated CaOx formation and dissolution in the presence of citrate. a) The particle forms with a diameter of ≈20 nm, and increases in contrast throughout 0–3 s. At $t = 3$ s, the particle develops 90° corners. This particle fluctuates in diameter, contrast, and corner sharpness before dissolving at $t = 17.3$ s. b) MD simulations shows aggregation of calcium and oxalate ions during nucleation. In contrast, in MD simulations show that calcium:citrate interactions prevent nucleation of CaOx. All TEM images were collected at the same magnification in the same area. c) The local water molecule concentration in the MD simulations in the absence of citrate and in the presence of citrate. A representative aggregation of CaOx formed without citrate illustrates the presence of water molecules (blue) around a CaOx particle in the inset. Oxalate anions are indicated in green, and calcium cations in orange. In the presence of citrate CaOx has a much higher water molecule to calcium ratio along the *Y*-axis, suggesting an increase in the hydration state. Further, there is reduced aggregation along the *X*-axis. In the inset smaller CaOx clusters formed in the presence of citrate illustrate a higher local water molecule to calcium ratio as compared to absence of citrate. Citrate anions are indicated in red. The scale bar in (a) is 20 nm, 5 nm in (b), and 1 nm in (c).

Other calcium salts have been also observed to form via multiple nucleation pathways.[31,70,71] While Figures 1 and 2 were collected from the same GLC zone, local variations in the ionic saturation, temperature, or entropy of the solution may also influence the observed crystallization pathway.[40,72] These factors, estimated in SI and described in other TEM works, may vary at the nanoscale to produce the observed changes in the crystallization pathway.[31,65,70,71,73–78]

2.3. In Situ TEM Studies of CaOx Dissolution in the Presence of Citrate

GLCs containing both CaOx and citrate (**Figure 3**, Figure S7, and Video S6, Supporting Information) display markedly different CaOx crystal nucleation for most of the particles observed to nucleate. In Figure 3a, a particle first appears at ≈20 nm in diameter with very low contrast throughout 0 to 1.3 s. A contour plot of these contrast changes over time has been included in Figure S8, Supporting Information. From 1.3 to 3 s, the particle contrast increases while remaining the same diameter (Figure 3, Figure S7, and Video S6, Supporting Information). The particle then dissolves from 3 to 17.3 s (Figure 3, Figure S7, and Video S6, Supporting Information). Several underlying phenomena may explain these observations. First, the particle may grow in the z direction only, without apparent growth in the image plane in Figure 3. This changes the contrast due to increased thickness. Second, the particle may be rotating. This rotation may cause changes in the diffraction contrast of the particle if the particle is crystalline. Third, the particle may be dissolving and reforming at the same location. This may occur due to high local concentrations of ions. The contour plot of the growth phase (Figure S8, Supporting Information) resembles previous observations of $CaCO_3$ growth from dense liquid droplets.[64] Here, high ionic concentrations may not be visible in Figure 3. Regardless of the underlying mechanism of particle appearance and disappearance, here citrate limits the formation of CaOx to ≈20 nm in diameter. It is unclear if the particles are crystalline, semi-crystalline, or amorphous, due to the limited resolution of the figure.

Nucleation of CaOx from a supersaturated solution without and with 0.1 M citrate were modeled by MD simulations (Figure 3b,c, and Videos S7 and S8, Supporting Information). While the magnification of experimental figures exceeds many previous works on low-contrast carbon-based particles, liquid-cell TEM is limited in its resolution due to the thickness of the sample. MD simulations are limited to small volumes and short timescales due to the current limitations of

© 2021 Wiley-VCH GmbH

modern computers. Thus, the MD approach provides insight what can be observed in liquid-cell TEM rather than direction comparisons. In the MD simulations, in the absence of citrate, CaOx aggregated to form amorphous clusters. These clusters then continued increasing in size and combining with other clusters (Figure 3b). However, when citrate was present, the calcium ions interacted with the citrate and formed small and unstable complexes (Figure 3b). The alternative calcium:citrate interactions prevented stable precipitation of CaOx, similar to the CaOx and citrate solution in Figure 3. This effect occurs because the tridentate citrate anion, with three carboxylic acids groups capable of accepting calcium cations, exhibits stronger Ca:O bonds than the bidentate oxalate.[35,38] The MD simulations were also performed at higher pressure to control for possible changes in pressure due to GLC encapsulation (Figures S8, and S10, and Note S3, Supporting Information).

The alternative calcium:citrate interactions thus reduce the free calcium present which prevents stable formation of CaOx (Figure 3c). However, calcium citrate does not precipitate since the overall structure of calcium citrate is less stable than CaOx (Note S1, Supporting Information).[35] Thus, throughout Figure 3, an equilibrium between the calcium:citrate and calcium:oxalate exists, which prevents stable precipitation of CaOx. Excess calcium ions in the solution temporarily overcome the formation of soluble calcium:citrate complexes, which form CaOx nanoparticles (Figure 3, and Video S6, Supporting Information). However, the interactions of calcium with citrate dissolves the CaOx particles, which leads to the cyclic formation and dissolution of unstable CaOx experimentally observed in Figure 3a and modeled in Figure 3b,c. This supports the third possible explanation for the phenomena observed in Figure 3a, wherein a high ionic concentration forms, condenses into a 20 nm diameter particle, before dissolving due to the citrate.

2.4. Formation of COD in the Presence of Citrate

As previously mentioned, citrate may increase the solubility of CaOx. Previous works have reported this possibility at different concentrations of CaOx and citrate. The increase in the solubility of CaOx was only reported to be ≈0.4 mM of CaOx in previous works.[35] Here, much higher concentrations of CaOx were used, which may alter the effect of citrate.[35] The GLC confinement may alter the local ion concentrations, which permits the particle dynamics observed in Figure 3a.[35,79,80] The nucleation of CaOx or calcium citrate at higher ionic concentrations must also be considered. At sufficiently high ion concentrations the chelating effect of citrate may be overcome and precipitation of CaOx observed as previously documented.[35]

In addition to the inhibitory effect of citrate, discussed above, MD simulations also determined the correlation between the ratio of water molecules and calcium ions present in each cluster and the size of that cluster (determined by the number of calcium ions in the respective cluster) (Figure 3c). In both the absence and presence of citrate the above ratio reached a limiting value with increasing cluster sizes (Figure 3c). Without citrate, this limiting value is around 5, whereas with citrate it increases to 12.5 (Figure 3c). In the presence of citrate, we can expect that the finger-like clusters eventually collapse and capture more waters than do the round compact clusters formed in the absence of citrate. This suggests that the presence of citrate may increase the hydration state of the CaOx formed (Figure 3c), in agreement with experimental observations (COD formation observed in the presence of citrate).

In addition to the dissolution of CaOx previously observed at equilibrium in Figure 3 (Video S6, Supporting Information), other GLCs containing CaOx and citrate showed formation of irregular nanoparticles (**Figure 4**a–d, Figure S10, and Video S6, Supporting Information). Unlike Figures 1 (Video S1, Supporting Information) and Figure 2 (Video S4, Supporting Information), characteristic crystal morphologies were not observed here (Figure 4a, Figure S10, and Video S9, Supporting Information). However, SAED of CaOx particles formed in the presence of citrate (Figure 4b) shows the presence of polycrystalline COD overlapped with graphene peaks.[81–83] The individual, distinct spots identify the (100) and (210) planes of graphene in Figure 4b.[81,82] The side by side dots in the SAED pattern indicate the presence of two layers of graphene (Figure 4b).[82] This shows that the GLC consists of a lower single layer of graphene under the sample, while another single layer of graphene covers the sample to encapsulate it (Figure 4b). Circles rather than individual diffraction spots indicate the presence of many crystals which make up the overall polycrystalline structure and identify the formation of COD rather than COM (Figure 4b and Video S9, Supporting Information).[81–83] The presence of COD shows an increase in the hydration state from COM, consistent with MD simulations (Figure 3b,c).

The formation of COD in the presence of citrate observed in GLC was also supported by ex situ experiments. SEM imaging showed CaOx morphologies representative of COD, while XRD confirmed the crystal structure of COD (Figure 4c,d).[83] EDS chemical analysis identified the oxygen signal increase from the expected 5:1 O:Ca in COM synthesized in the absence of citrate (Figure 4e–g). In the presence of citrate, there was a 6:1 O:Ca ratio indicative of the formation of COD (Figure 4e–g). EELS showed slightly lower values as compared to EDS, which is likely due to electron beam sample damage (Figure 4e–g). EELS did however confirm the increased oxygen signal (Figure 4e–g). EDS mapping showed no significant background oxygen signal in the ex situ samples (Figure S12, Supporting Information).

3. Discussion

Here, the nanoscale nucleation pathway of CaOx and the effect of a molecular modifier (citrate) was directly observed in real time and structurally analyzed by in situ liquid-cell TEM imaging. MD studies provided additional insight into the mechanism by which citrate alters the crystal structure and hydration state. The first portion of this study was dedicated to in situ liquid-cell TEM investigation of crystallization pathways of CaOx without citrate. Previous works reported that COM exhibits a monoclinic crystal structure.[1] Preferential facet growth of the monoclinic crystal however produces unique crystal morphologies.[1] Here, comparison of Figure 1 (Figure S1 and Video S1, Supporting Information) and Figure 2 (Figure S4 and Video S2, Supporting Information) reveals that CaOx may mineralize via two energetically feasible pathways.

© 2021 Wiley-VCH GmbH

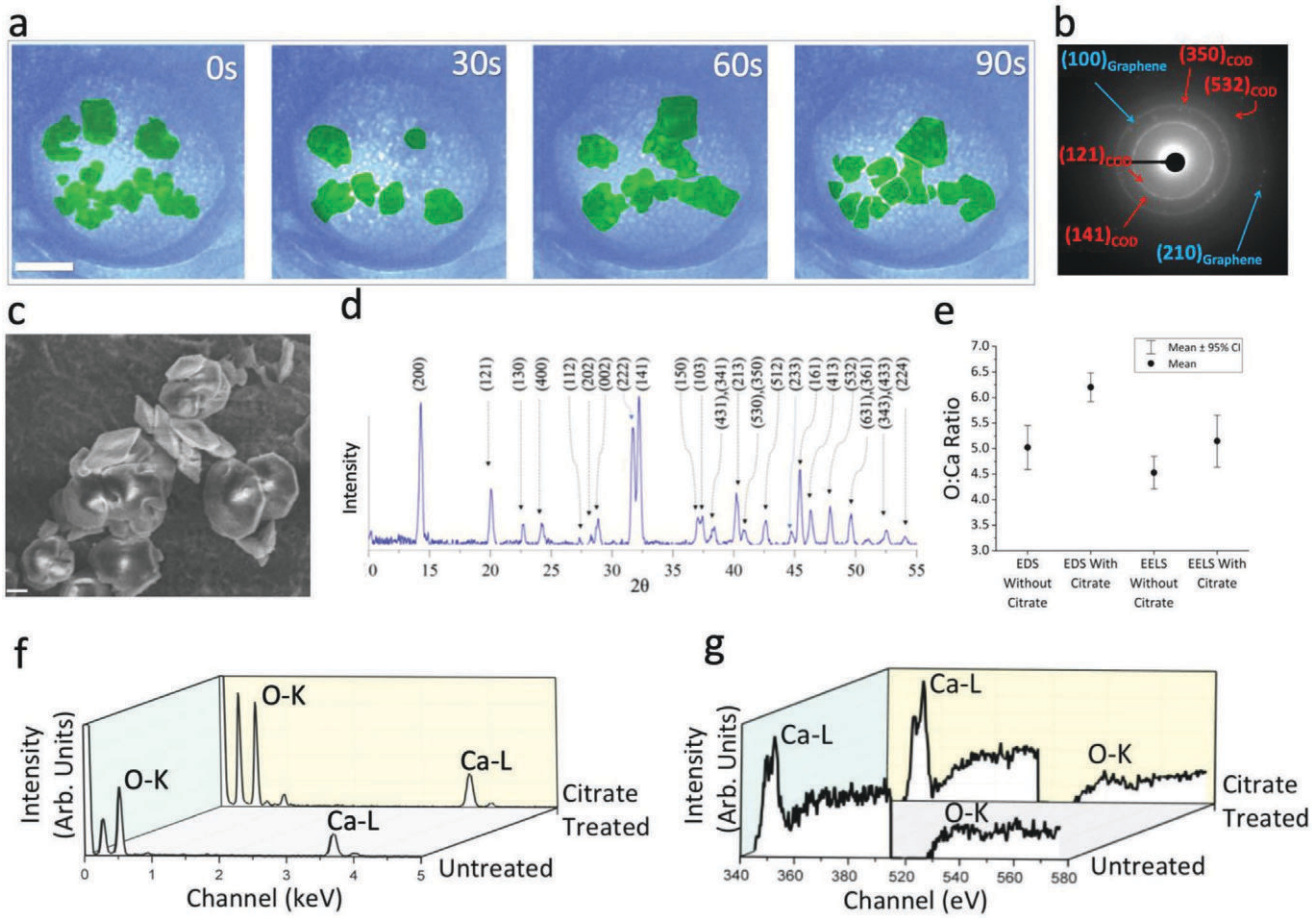


Figure 4. Formation of COD in the presence of citrate is observed both in situ and ex situ. a) A time series shows motion of CaOx nanoparticles within GLC. b) SAED shows overlapped crystalline graphene and polycrystalline COD diffraction peaks as collected from the GLC sample. c) SEM imaging of CaOx synthesized in the presence of citrate shows the bipyramidal morphology indicative of COD. d) XRD of bulk CaOx samples synthesized in the presence of citrate shows the formation of COD. e) EDS and EELS spectra of O:Ca ratios from ten ex situ samples without citrate and with citrate are displayed. The EDS and EELS data show a consistent increase in the O:Ca ratio in the presence of citrate. f) A representative EDS spectra from samples with and without citrate show an increase in the oxygen signal in the presence of citrate. g) Comparison between the EELS spectra of ex situ CaOx without citrate and with citrate shows an increase in the O:Ca ratio in the presence of citrate. The scale bar in (a) is 100 nm. In (c) the scale bar is 500 nm.

The rhombohedral COM seems to nucleate classically, while the rectangular COM nucleates by multiphase non-classical pathways (**Figure 5**).[84,85]

The presence of citrate alters the solubility, hydration state, crystal structure, and morphology of the CaOx crystals during the nucleation process. Citrate-induced changes in the formation of CaOx were previously predicted to occur by interaction with amorphous precursors,[29] polynuclear complexes,[29] or by step-pinning of crystal facets as in the C–V model.[37] Ruiz–Agudo et al.[29] showed that CaOx was inhibited by citrate due to citrate coating growing amorphous particles to prevent further aggregation. Here, it is difficult to find evidence for such coating. Instead, it was observed that the dihydrate form of CaOx can become more stable due to integration of water molecules in the CaOx aggregates. These differences may arise due to variations in the reagent concentrations, background electrolytes, or addition of additives reported in many studies.

Future studies may implement similar approaches to provide mechanistic insight into the role of trace elements and molecular modifiers on the nucleation of CaOx. Previous works have documented a wide range of trace elements and materials that alter the crystal structure and morphology of CaOx.[86] These materials include copper, magnesium, zinc, manganese, and ethylenediaminetetraacetic acid, among others.[86] Future liquid-cell TEM studies are encouraged to explore the effect of other additives which may alter nucleation pathways of CaOx.

In this work, the effects of the electron beam and pressure due to encapsulation in GLC were considered and shown to have minimal effects on the crystallization pathways of CaOx (see Notes S2 and S3, Figures S1, S3, S8, and S9, and Videos S1–S8, Supporting Information). Significant differences in CaOx particles were not observed in separate areas of the GLCs, in different GLCs, under different electron dose rates, or within different electron microscopes (Figure S1, Note S2, and Videos S1 and S3, Supporting Information). The in situ TEM results were supported by MD simulations (Figures 3, Figures S8–S10, and Videos S6 and S7, Supporting Information) and ex situ studies (Figure 4, Figures S7 and S11, Supporting

© 2021 Wiley-VCH GmbH

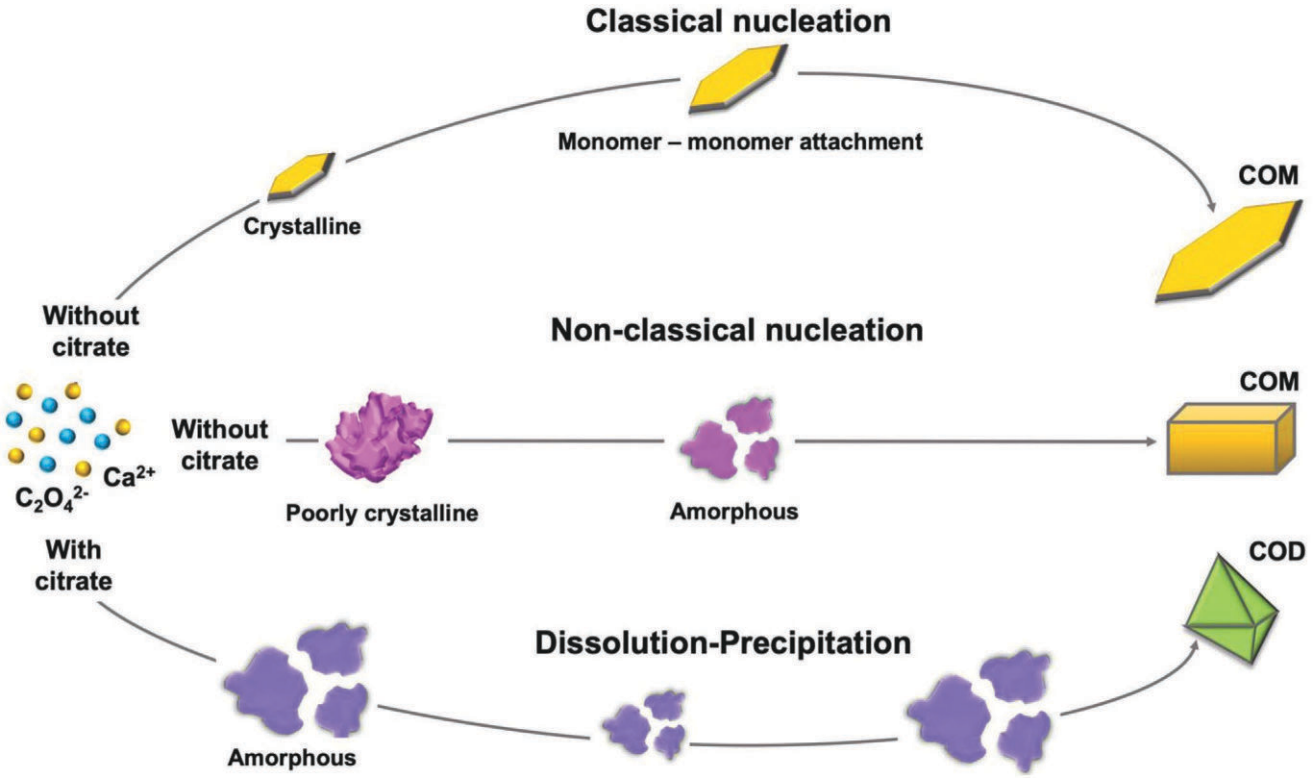


Figure 5. Nucleation pathways of CaOx. In the classical nucleation pathway, a small crystal forms and grows by monomer–monomer attachment to form rhombohedral COM crystal. In the non-classical nucleation pathway, a poorly crystalline particle forms, partially dissolves, and reforms as square COM. Finally, in the presence of citrate, CaOx forms amorphous precursors, which dissolves, reforms, and then forms COD.

Information), which indicate that the CaOx crystallization in GLC reflects the crystallization of CaOx in the absence of the electron beam.

Here, real-time liquid-cell TEM studies show the nanoscale nucleation of CaOx via two pathways. Classical nucleation leads to the formation of rhombohedral COM, the most thermodynamically favorable crystal structure of CaOx, whereas rectangular COM forms via non-classical nucleation. The dependence of the final crystal structure on the nanoscale nucleation pathway shown here demonstrates the importance of the initial conditions which control particle nucleation pathways. These conditions may include factors such as local ion mobility and diffusion within the solution. Real-time liquid-cell TEM studies and MD simulations show that citrate buffers formation of stable formation of CaOx. This inhibition occurs via transient formation of soluble calcium:citrate complexes. At high calcium concentrations, however, the inhibiting effect of citrate is overcome, which causes formation of COD. MD dynamics show that the formation of COD rather than COM is induced during the initial nucleation of the crystal, during which the citrate draws more water into the forming CaOx nucleus.

4. Experimental Section

Sample Preparation: CaOx was synthesized by chemical reaction between sodium oxalate (NaOx) (Sigma-Aldrich) and calcium chloride ($CaCl_2$) (Fisher Chemical) in picopure water (WaterOmniTrace Ultra, EMD Millipore Corporation): $Na_2C_2O_4 + CaCl_2 \rightarrow CaC_2O_4 + 2NaCl$. This implementation of picopure water prevents the addition of possible additives and background ions. Sodium citrate was added to the solutions to achieve a final concentration of 0.1 M NaOx, 0.1 M $CaCl_2$, and 0.1 M sodium citrate concentrations. In ex situ samples, the CaOx formed immediately. CaOx was centrifuged within 10 min to separate the solid sample from the supernatant which contained NaCl. This would also have removed trace amounts of dissolved CaOx as detailed in Tables S1–S14, Supporting Information. After the supernatant was removed, the CaOx particles were rehydrated in DI water. The samples were then mixed, centrifuged, and the supernatant removed to rinse the sample. This process stopped the chemical reaction and prevented the formation of NaCl and citrate solution immediately upon mixing, prior to any product formation, at equilibrium, with consideration of products formed. In in situ samples, the CaOx samples were not rinsed, since the in situ samples remained in liquid, which prevented the formation of NaCl (Figure 4c,d, Tables S12 and S13, Supporting Information).

Visual MINTEQ software described the expected saturation state, described factors such as the pH, ionic strength, dissolved species, and possible solid products. Four conditions were considered: 1) the CaOx solution immediately upon mixing, prior to any product formation, 2) the CaOx and citrate solution immediately upon mixing, prior to any product formation, 3) the CaOx solution and citrate at equilibrium, with consideration of products formed, and 4) the CaOx solution at equilibrium, with consideration of products formed. The full input parameters and results are included in Tables S1–S14, Supporting Information. The formation of COM, COD, and COT were considered as possible products. ACO was excluded since it has only been reported to form in the presence of additives absent in this work.[20] Calcium citrate, sodium chloride, and calcium carbonate were included in the Visual MINTEQ model as possible phases but did not form in the

© 2021 Wiley-VCH GmbH

simulations (Note S1, Supporting Information). The saturation states of the solutions are summarized in Table 1. The Visual MINTEQ model was based on theoretical models and might not reflect kinetic factors.

In Situ GLC-TEM Imaging: In situ TEM imaging was achieved by encapsulation of different CaOx samples between two layers of graphene, which were prepared by adding NaOx, $CaCl_2$, and sodium citrate solutions to microcentrifuge tubes and then combining them as previously discussed. Approximately 0.5 µL of the solution was added to a graphene coated grid. A second graphene coated grid was placed graphene side down on the liquid sample; Textor et al. provided an extensive review of this GLC synthesis process.[87] The grid was then placed into a TEM sample holder, which was placed into a vacuum pump to remove any liquid that was not encapsulated in GLC from the TEM holder. The sample was then imaged in TEM at 80 kV.

The absorbed electron dose rate was calculated from:

$$\Psi = \frac{10^5 SI}{\pi a^2} \tag{4}$$

where S is the stopping power $\left(\frac{\text{MeVcm}^2}{\text{g}}\right)$, I is the current (amperes), a is the radius of the electron beam (meters), and 10^5 is a constant in units of $\frac{\text{m}^2\ \bar{\text{e}}\ \text{Gy g}}{\text{cm}^2\ \text{MeV C}}$ that converts SI units to Grays s^{-1}.[65] The absorbed electron dose rate was between 3×10^9 and 2.24×10^{12} Gy s^{-1}. The pH and radiolysis species analyses were based on previous works.[65] Time scales reported in Figures 1–4, Figures S1, S3–S5, S7, S11, and S13 and Videos S1–S6 and S9, Supporting Information, consider the start of the video to be $t = 0$, which occurs after preparing the sample-containing GLC, loading the GLC into the microscope, aligning the microscope, and locating a particle or area of interest. This process took between ten minutes to an hour. Due to the high reaction rate, the CaOx solutions reached chemical equilibrium prior to GLC synthesis. The crystal formation observed in Figures 1–4, Figures S1, S3–S5, S11, and S13 and Videos S1–S6 and S9, Supporting Information, occurred upon the electron beam exposure of the area of the GLC in the image. This electron beam exposure generated radiolytic species. Thus, the electron beam exposure was the primary consideration in determining the dynamics of the CaOx particle formation (Note S2, Supporting Information).

GLC samples containing CaOx or CaOx and citrate were observed in a JEOL 1220 TEM (Figure 1–3, Figures S1, S4, and S7, and Videos S1, S4, and S6, Supporting Information) and a JEOL ARM 200CF STEM operated in TEM (Figure 4, Figures S4–6, and S11, and Videos S2, S3, S5, S8, and S9, Supporting Information). SAED of GLCs was collected by the JEOL ARM 200CF STEM. Particle analysis of Figure 1 was performed as described by Kennedy et al., which indicated the image resolution was ≈2.5 nm or less (Figure S13, Supporting Information).

MD1 Modeling of CaOx Formation: MD simulations were performed with NAMD2.12.[88] Water molecules were described using TIP3P model.[89] Monoatomic ions were modeled by their Lennard–Jones parameters and integral charges.[90] Parameters for citrate and oxalate ions were determined using MP2/6-31G*// MP2/6-31G* level of theory, in implicit water solvent through Gaussian program,[91] using VMD force field toolkit.[92] In all simulations, the particle-mesh Ewald method[93] was used for evaluation of long-range Coulomb interactions. Long-range interactions were evaluated every 1 (van der Waals) and 2 (Coulombic) time steps. The simulations were performed in the NpT ensemble at a constant temperature of 310 K, constant pressure (varied for different simulations) and a Langevin constant of $\gamma_{\text{Lang}} = 1.00\ \text{ps}^{-1}$. The pure CaOx simulations had the same number of water, calcium, oxalate ions, such that [CaOx] = 0.125 M at 1 atm. There were a total of 254 oxalate ions in all simulations. Simulations with citrate ions had the same number of citrate and oxalate ions. Spectator ions were also added into the system in order to replicate experimental conditions. The systems (citrate present or absent) differed by applied pressures of 1 and 100 atm. MD simulations at 100 atm were included to control for the possible increase in pressure due to GLC encapsulation (Note S3, Supporting Information). The 100 atm pressure was selected since it was an order of magnitude greater than pressure predicted by previous studies.[75] The systems were minimized for 5000 steps and then pre-equilibrated for 2 ns, with a time step set to 2.0 fs. During minimization and pre-equilibration, one carbon atom on each oxalate and citrate (if applicable) molecule was harmonically constrained in order to allow these molecules to rotate, but not diffuse. There were no constraints during the simulations, which ran for 100 ns and with a time step of 1.0 fs.

During the evaluation of number of water molecules within clusters, it was assumed that a cluster had at least one calcium ion and one oxalate or citrate molecule, which had at least one of their atoms within 2.5 Å of that calcium ion. Clusters were determined by selecting a calcium or oxalate ion and finding the neighboring calcium, oxalate, or citrate ions within 2.5 Å. This process was repeated until the whole cluster was determined. Iterations ended when no new neighbors were found. After the cluster size was determined, the number of water molecules that were within 2.5 Å of any calcium, oxalate, or citrate molecule in the final cluster was determined. In order to eliminate effects related to a finite simulation box, it was determined whether any molecule in the final cluster was within 4.5 Å of the boundary of simulation box. If there was a cluster close to the boundary of the box, the entire cluster and neighboring water molecules were displaced and the calculations were repeated. The sizes of clusters were determined by the number of calcium ions in those clusters. Evaluations of cluster sizes were determined for every 1.00 ns, due to memory limitations. The computational power of modern computers limited the volume of the MD simulations to several nanometers.

Scanning Electron Microscopy: CaOx samples formed in the absence of citrate and CaOx samples formed in the presence of citrate were added in 50 µL volumes to copper tape upon an SEM stub and air-dried overnight. Samples were gold sputtered for 4 min at 20 eV. SEM images were collected at 2 to 3 keV at working distances of 13 to 20 mm with a RAITH100 eLine EBL.

X-Ray Diffraction: A Bruker D8 Discover XRD system was used to collect XRD data. The diffractometer was operated at 40.0 kV and 40.0 mA at a 2θ range of 5 to 60° with a 0.02 step size, and exposure time of 1 s/step.

Energy-Dispersive X-Ray Spectroscopy: STEM-EDS data was collected to determine the elemental composition of the samples. The JEOL ARM 200CF STEM used was equipped with Oxford X-max 100TLE windowless SDD X-Ray detectors capable of detecting oxygen. Calcium and oxygen peaks were expected, while potential contaminants such as sodium and chloride were monitored. The 0–20 kV energy range was examined while 0–10 kV was used to obtain a more precise data collection. EDS mapping of the crystal was implemented to minimize the local electron dose, which was observed to damage the sample and to alter the Ca:O ratio in point or line EDS collection. Primary detection of elements was performed with extended collection time with an electron dose rate of 1.8 $\bar{\text{e}}\ \text{Å}^{-2}\text{s}$ and a total electron dose of $2.8 \times 10^3\ \text{Å}^{-2}$. Quantitative Ca:O data used to produce the reported Ca:O ratios was collected near the edge of 200 to 500 nm particles. Edge collection and collection from smaller particles reduced scattering within the particle and subsequent production of damaging secondary electrons. EDS mapping was collected from ≈200 by 200 nm areas with electron dose rates between 20 and 40 $\bar{\text{e}}\ \text{Å}^{-2}\text{s}$. Total electron doses were between 2×10^2 and $8 \times 10^2\ \bar{\text{e}}\ \text{Å}^{-2}$, with an average of 26.2 $\bar{\text{e}}\ \text{Å}^{-2}\text{s}$ and an averaged total of $8 \times 10^2\ \bar{\text{e}}\ \text{Å}^{-2}$ per EDS map. These high electron dose rates maximized the EDS signal while minimizing the total damage and incurred elemental loss over the ≈10 s collection time.

Electron Energy Loss Spectroscopy: The STEM-EELS data was acquired using a Hitachi HD2300 STEM microscope operating at 200 kV. The energy range of 270–577.2 eV were examined with 0.35 eV energy dispersion and EELS aperture of 3 mm. Energy windows of 50 eV were used to compare the ratio of O:Ca using the O K edge and Ca L edge. Electron exposure was set to 15 s. The EELS data collection electron dose rate was 38 $\bar{\text{e}}\ \text{Å}^{-2}\text{s}$ while the total dose was 573 $\bar{\text{e}}\ \text{Å}^{-2}$.

© 2021 Wiley-VCH GmbH

Supporting Information

Supporting Information is available from the Wiley Online Library or from the author.

Acknowledgements

This work made use of instruments in the Electron Microscopy Services (Research Resources Center, UIC). The authors thank UIC the Nanotechnology Core Facility (NCF) for their assistance in order to use their equipment. This project was financially supported by a grant from the National Science Foundation (NSF-DMR Award No. 1710049). T. Shokuhfar is grateful to NSF-CAREER award DMR-1564950.

Conflict of Interest

The authors declare no conflict of interest.

Author Contributions

D.J.B., E.F., and P.R. contributed equally to this work. This study was conceptualized by D.J.B., T.S., and R.S.-Y. The manuscript, figures, and supporting information were prepared by D.J.B. and P.R. with editing and contributions by E.F., A.P., R.S.-Y., and P.K. D.J.B. designed all in situ experiments and prepared samples. Figures 1 and 2, Figures S1, S4, and S13 and Videos S1 and S4, Supporting Information, and the EELS data in Figure 4e,g were collected by E.F. D.J.B. collected Figures 3a, and 4a–c, the EDS data in Figure 4e,f, Figures S3, S6a,b, S8, S11, S12, Tables S1–S14, and Videos S2, S3, S6, and S9, Supporting Information. P.R. performed all MD simulations shown in Figure 3b,c, Figures S9 and S10, and Videos S7 and S8, Supporting Information. A.P. collected Figure S5, Supporting Information. T.T. and Y.B. contributed to data processing from Figures 1 and 2 (unpublished). J.K.O. contributed to data processing Figure 3 (unpublished) and to repetition of ex situ CaOx experiments to produce statistical data. T.F. collected Figure 4d and Figure S6c, Supporting Information. S.N. advised proper SEM sample preparation and SEM imaging conditions for Figure 4c and Figure S6a,b, Supporting Information. Figure 5 was produced by L.V.S. and D.J.B. This manuscript was advised by R.S.-Y., T.S., and P.K. All authors have given approval to the final version of the manuscript.

Data Availability Statement

Data available on request from the authors.

Keywords

calcium oxalate, graphene liquid cells, liquid-cell TEM, nucleation, growth mechanisms

Received: September 10, 2020
Revised: January 27, 2021
Published online:

[1] W. P. Hartl, H. Klapper, B. Barbier, H. J. Ensikat, R. Dronskowski, P. Müller, G. Ostendorp, A. Tye, R. Bauer, W. Barthlott, *Can. J. Bot.* **2007**, *85*, 501.
[2] J. A. Raven, H. Griffiths, S. M. Glidewell, T. Preston, *Proc. R. Soc. London, Ser. B* **1982**, *216*, 87.
[3] P. J. White, M. R. Broadley, *Ann. Bot.* **2003**, *92*, 487.
[4] M. A. Webb, *Plant Cell* **1999**, *11*, 751.
[5] V. R. Franceschi, P. A. Nakata, *Annu. Rev. Plant Biol.* **2005**, *56*, 41.
[6] L. A. J. Garvie, *Naturwissenschaften* **2006**, *93*, 114.
[7] A. Morita, O. Yanagisawa, S. Takatsu, S. Maeda, S. Hiradate, *Phytochemistry* **2008**, *69*, 147.
[8] G. Martin, M. Guggiari, D. Bravo, J. Zopfi, G. Cailleau, M. Aragno, D. Job, E. Verrecchia, P. Junier, *Environ. Microbiol.* **2012**, *14*, 2960.
[9] P. R. Ryan, E. Delhaize, D. L. Jones, *Annu. Rev. Plant Physiol. Plant Mol. Biol.* **2001**, *52*, 527.
[10] A. A. Gorbushina, W. E. Krumbein, M. Volkmann, *Astrobiology* **2002**, *2*, 203.
[11] F. L. Coe, A. Evan, E. Worcester, *J. Clin. Invest.* **2005**, *115*, 2598.
[12] T. Umekawa, Y. Hatanaka, T. Kurita, S. R. Khan, *J. Am. Soc. Nephrol.* **2004**, *15*, 635.
[13] F. Grases, A. Costa-Bauzá, M. Ramis, V. Montesinos, A. Conte, *Scand. J. Urol. Nephrol.* **2003**, *37*, 482.
[14] A. Trinchieri, F. Ostini, R. Nespoli, F. Rovera, E. Montanari, G. Zanetti, *J. Urol.* **1999**, *162*, 27.
[15] J. M. Soucie, M. J. Thun, R. J. Coates, W. McClellan, H. Austin, *Kidney Int.* **1994**, *46*, 893.
[16] O. Mohamed, M. Monga, J. C. Calle, *J. Nephrol. Ther.* **2015**, *5*, 1000198.
[17] F. Grases, A. Millan, A. Conte, *Urol. Res.* **1990**, *18*, 17.
[18] X. Sheng, *J. Am. Soc. Nephrol.* **2005**, *16*, 1904.
[19] W. Heijnen, W. Jellinghaus, W. E. Klee, *Urol. Res.* **1985**, *13*, 281.
[20] J. Ihli, Y.-W. Wang, B. Cantaert, Y.-Y. Kim, D. C. Green, P. H. H. Bomans, N. A. J. M. Sommerdijk, F. C. Meldrum, *Chem. Mater.* **2015**, *27*, 3999.
[21] A. Gehl, M. Dietzsch, M. Mondeshki, S. Bach, T. Häger, M. Panthöfer, B. Barton, U. Kolb, W. Tremel, *Chem. - Eur. J.* **2015**, *21*, 18192.
[22] M. Hajir, R. Graf, W. Tremel, *Chem. Commun.* **2014**, *50*, 6534.
[23] J. P. Kavanagh, L. Jones, P. N. Rao, *Clin. Sci.* **2000**, *98*, 151.
[24] J. P. Kavanagh, L. Jones, P. N. Rao, *Urol. Res.* **1999**, *27*, 231.
[25] J. P. Kavanagh, *Urol. Res.* **2006**, *34*, 139.
[26] E. Weber, A. Verch, D. Levy, A. N. Fitch, B. Pokroy, *ChemistrySelect* **2016**, *2*, 132.
[27] A. Shebanova, T. Ismagulova, A. Solovchenko, O. Baulina, E. Lobakova, A. Ivanova, A. Moiseenko, K. Shaitan, V. Polshakov, L. Nedbal, O. Gorelova, *Protoplasma* **2017**, *254*, 1323.
[28] J. C. Lieske, H. Swift, T. Martin, B. Patterson, F. G. Toback, *Proc. Natl. Acad. Sci. U. S. A.* **1994**, *91*, 6987.
[29] E. Ruiz-Agudo, A. Burgos-Cara, C. Ruiz-Agudo, A. Ibañez-Velasco, H. Cölfen, C. Rodriguez-Navarro, *Nat. Commun.* **2017**, *8*, 768.
[30] E. Weber, D. Levy, M. B. Sasson, A. N. Fitch, B. Pokroy, *RSC Adv.* **2015**, *5*, 98626.
[31] M. H. Nielsen, S. Aloni, J. J. De Yoreo, *Science* **2013**, *218*, 213.
[32] J. A. Wesson, E. M. Worcester, J. H. Wiessner, N. S. Mandel, J. G. Kleinman, *Kidney Int.* **1998**, *53*, 952.
[33] C. D. Scales, A. C. Smith, J. M. Hanley, C. S. Saigal, *Eur. Urol.* **2012**, *62*, 160.
[34] E. S. Hyams, B. R. Matlaga, *Transl. Androl. Urol.* **2014**, *3*, 278.
[35] D. J. Kok, S. E. Papapoulos, L. J. M. Blomen, O. L. M. Bijvoet, *Kidney Int.* **1988**, *34*, 346.
[36] M. L. Weaver, S. R. Qiu, J. R. Hoyer, W. H. Casey, G. H. Nancollas, J. J. De Yoreo, *J. Cryst. Growth* **2007**, *306*, 135.
[37] L. Wang, J. J. De Yoreo, X. Guan, S. R. Qiu, J. R. Hoyer, G. H. Nancollas, *Cryst. Growth Des.* **2006**, *6*, 1769.
[38] J. Chung, I. Granja, M. G. Taylor, G. Mpourmpakis, J. R. Asplin, J. D. Rimer, *Nature* **2016**, *536*, 446.
[39] J. Tersoff, R. M. Tromp, *Phys. Rev. Lett.* **1993**, *70*, 2782.
[40] J. J. De Yoreo, P. U. P. A. Gilbert, N. A. J. M. Sommerdijk, R. L. Penn, S. Whitelam, D. Joester, H. Zhang, J. D. Rimer, A. Navrotsky,

© 2021 Wiley-VCH GmbH

J. F. Banfield, A. F. Wallace, F. M. Michel, F. C. Meldrum, H. Cölfen, P. M. Dove, *Science* **2015**, *349*, aaa6760.
[41] R. De Bellis, M. P. Piacentini, M. A. Meli, M. Mattioli, M. Menotta, M. Mari, L. Valentini, L. Palomba, D. Desideri, L. Chiarantini, *PLoS One* **2019**, *14*, e0218734.
[42] V. Thongboonkerd, T. Semangoen, S. Chutipongtanate, *Clin. Chim. Acta* **2006**, *367*, 120.
[43] D. N. Petsev, K. Chen, O. Gliko, P. G. Vekilov, *Proc. Natl. Acad. Sci. U. S. A.* **2003**, *100*, 792.
[44] R. Demichelis, P. Raiteri, J. D. Gale, D. Quigley, D. Gebauer, *Nat. Commun.* **2011**, *2*, 590.
[45] J. L. Zryd, W. R. Burghardt, *J. Appl. Polym. Sci.* **1995**, *57*, 1525.
[46] Q. Hu, M. H. Nielsen, C. L. Freeman, L. M. Hamm, J. Tao, J. R. I. Lee, T. Y. J. Han, U. Becker, J. H. Harding, P. M. Dove, J. J. De Yoreo, *Faraday Discuss.* **2012**, *159*, 509.
[47] N. D. Loh, S. Sen, M. Bosman, S. F. Tan, J. Zhong, C. A. Nijhuis, P. Král, P. Matsudaira, U. Mirsaidov, *Nat. Chem.* **2017**, *9*, 77.
[48] A. Navrotsky, *Proc. Natl. Acad. Sci. U. S. A.* **2004**, *101*, 12096.
[49] S. R. Qiu, A. Wierzbicki, E. A. Salter, S. Zepeda, C. A. Orme, J. R. Hoyer, G. H. Nancollas, A. M. Cody, J. J. De Yoreo, *J. Am. Chem. Soc.* **2005**, *127*, 9036.
[50] R. W. Friddle, M. L. Weaver, S. R. Qiu, A. Wierzbicki, W. H. Casey, J. J. De Yoreo, *Proc. Natl. Acad. Sci. U. S. A.* **2010**, *107*, 11.
[51] K. R. Cho, E. A. Salter, J. J. De Yoreo, A. Wierzbicki, S. Elhadj, Y. Huang, S. R. Qiu, *CrystEngComm* **2013**, *15*, 54.
[52] T. Jung, X. Sheng, C. K. Choi, W. S. Kim, J. A. Wesson, M. D. Ward, *Langmuir* **2004**, *20*, 8587.
[53] S. Guo, M. D. Ward, J. A. Wesson, *Langmuir* **2002**, *18*, 4284.
[54] S. Narayanan, E. Firlar, M. G. Rasul, T. Foroozan, N. Farajpour, L. Covnot, R. Shahbazian-Yassar, T. Shokuhfar, *Nanoscale* **2019**, *11*, 16868.
[55] E. Firlar, M. Ouy, A. Bogdanowicz, L. Covnot, B. Song, Y. Nadkarni, R. Shahbazian-Yassar, T. Shokuhfar, *Nanoscale* **2019**, *11*, 698.
[56] S. M. Ghodsi, C. M. Megaridis, R. Shahbazian-Yassar, T. Shokuhfar, *Small Methods* **2019**, *3*, 1900026.
[57] J. M. Yuk, J. Park, P. Ercius, K. Kim, D. J. Hellebusch, M. F. Crommie, J. Y. Lee, A. Zettl, A. P. Alivisatos, J. C. Meyer, C. O. Girit, M. F. Crommie, A. Zettl, C.-Y. Wen, V. Radmilovic, A. H. Zewail, N. de Jonge, F. M. Ross, M. J. Williamson, R. M. Tromp, P. M. Vereecken, R. Hull, F. M. Ross, H. Zheng, J. E. Evans, K. L. Jungjohann, N. D. Browning, I. Arslan, K. S. Novoselov, X. Li, J. N. Coleman, Z. Lee, A. Kolmakov, Y. A. Wu, J. C. Meyer, C. O. Girit, M. F. Crommie, A. Zettl, R. Erni, R. R. Nair, J. M. Yuk, K. Xu, P. Cao, J. R. Heath, X. Li, W. Regan, X. Xie, S. P. Koenig, N. G. Boddeti, M. L. Dunn, J. S. Bunch, J. C. Meyer, E. A. Stach, H. Zheng, S. A. Claridge, A. M. Minor, A. P. Alivisatos, U. Dahmen, X. Lu, M. Rycenga, S. E. Skrabalak, B. Wiley, Y. Xia, K. J. M. Bishop, C. E. Wilmer, S. Soh, B. A. Grzybowski, X. Lu, M. S. Yavuz, H.-Y. Tuan, B. A. Korgel, Y. Xia, P. Schapotschnikow, R. Pool, T. J. H. Vlugt, Z. Z. Fang, H. Wang, *Science* **2012**, *336*, 61.
[58] C. Wang, T. Shokuhfar, R. F. Klie, *Adv. Mater.* **2016**, *28*, 7716.
[59] C. Wang, Q. Qiao, T. Shokuhfar, R. F. Klie, *Adv. Mater.* **2014**, *26*, 3410.
[60] Q. Chen, J. M. Smith, J. Park, K. Kim, D. Ho, H. I. Rasool, A. Zettl, A. P. Alivisatos, *Nano Lett.* **2013**, *13*, 4556.
[61] D. J. Kelly, M. Zhou, N. Clark, M. J. Hamer, E. A. Lewis, A. M. Rakowski, S. J. Haigh, R. V. Gorbachev, *Nano Lett.* **2018**, *18*, 1168.
[62] X. Sheng, T. Jung, J. a Wesson, M. D. Ward, *Proc. Natl. Acad. Sci. U. S. A.* **2005**, *102*, 267.
[63] J. Li, *Microsc. Microanal.* **2006**, *12*, 698.
[64] Z. Liu, Z. Zhang, Z. Wang, B. Jin, D. Li, J. Tao, R. Tang, J. J. de Yoreo, *Proc. Natl. Acad. Sci. U. S. A.* **2020**, *117*, 3397.
[65] N. M. Schneider, M. M. Norton, B. J. Mendel, J. M. Grogan, F. M. Ross, H. H. Bau, *J. Phys. Chem. C* **2014**, *118*, 22373.
[66] J. W. Mullin, *Crystallization*, 4th ed., Butterworth-Heinemann, Oxford **2001**.
[67] D. Kashchiev, *Nucleation: Basic Theory with Applications*, 1st ed., Butterworth-Heinemann, Oxford **2000**.
[68] G. G. Libowitz, in *Treatise on Solid State Chemistry*, Vol. 1 (Ed: N. B. Hannay), Springer, Boston, MA, **1921**, p. 1335.
[69] T. Sugimoto, *Monodispersed Particles*, 1st ed., Elsevier, New York **2001**.
[70] K. He, M. Sawczyk, C. Liu, Y. Yuan, B. Song, R. Deivanayagam, A. Nie, X. Hu, V. P. Dravid, J. Lu, C. Sukotjo, Y. P. Lu, P. Krá, T. Shokuhfar, R. Shahbazian-Yassar, *Sci. Adv.* **2020**, *6*, eaaz7524.
[71] K. He, A. Nie, Y. Yuan, S. M. Ghodsi, B. Song, E. Firlar, J. Lu, Y. Lu, T. Shokuhfar, C. M. Megaridis, R. Shahbazian-Yassar, *ACS Appl. Nano Mater.* **2018**, *1*, 5430.
[72] J. J. De Yoreo, *Rev. Mineral. Geochem.* **2003**, *54*, 57.
[73] H. Cho, M. R. Jones, S. C. Nguyen, M. R. Hauwiller, A. Zettl, A. P. Alivisatos, *Nano Lett.* **2017**, *17*, 414.
[74] M. J. Berger, S. M. Seltzer, *Stopping Powers and Ranges of Electrons and Positrons*, 2nd ed., US Department of Commerce, Washington DC **1982**.
[75] E. Khestanova, F. Guinea, L. Fumagalli, A. K. Geim, I. V. Grigorieva, *Nat. Commun.* **2016**, *7*, 12587.
[76] J. M. Grogan, N. M. Schneider, F. M. Ross, H. H. Bau, *Nano Lett.* **2014**, *14*, 359.
[77] M. Denoual, V. Menon, T. Sato, O. De Sagazan, A. W. Coleman, H. Fujita, *Meas. Sci. Technol.* **2019**, *30*, 017001.
[78] J. T. Van Omme, H. Wu, H. Sun, A. F. Beker, M. Lemang, R. G. Spruit, S. P. Maddala, A. Rakowski, H. Friedrich, J. P. Patterson, H. H. Pérez Garza, *J. Mater. Chem. C* **2020**, *8*, 10781.
[79] E. Lopez-Fontal, A. Grochmal, T. Foran, L. Milanesi, S. Tomas, *Chem. Sci.* **2018**, *9*, 1760.
[80] R. Kröger, A. Verch, R. Kröger, A. Verch, *Minerals* **2018**, *8*, 21.
[81] W. Zhao, B. Xia, L. Lin, X. Xiao, P. Liu, X. Lin, H. Peng, Y. Zhu, R. Yu, P. Lei, J. Wang, L. Zhang, Y. Xu, M. Zhao, L. Peng, Q. Li, W. Duan, Z. Liu, S. Fan, K. Jiang, *Sci. Adv.* **2017**, *3*, e1603231.
[82] J. Li, X. Y. Wang, X. R. Liu, Z. Jin, D. Wang, L. J. Wan, *J. Mater. Chem. C* **2015**, *3*, 3503.
[83] V. Tszzorl, C. Dotvtbnecgbrrt, *Am. Mineral.* **1980**, *65*, 27.
[84] Y. H. Chen, H. P. Liu, H. Y. Chen, F. J. Tsai, C. H. Chang, Y. J. Lee, W. Y. Lin, W. C. Chen, *Kidney Int.* **2011**, *80*, 369.
[85] A. Millan, *Cryst. Growth Des.* **2001**, *1*, 245.
[86] F. Grases, C. Genestar, A. Millán, *J. Cryst. Growth* **1989**, *94*, 507.
[87] M. Textor, N. De Jonge, *Nano Lett.* **2018**, *18*, 3313.
[88] J. C. Phillips, R. Braun, W. Wang, J. Gumbart, E. Tajkhorshid, E. Villa, C. Chipot, R. D. Skeel, L. Kale, K. Schulten, *J. Comput. Chem.* **2005**, *26*, 1781.
[89] W. L. Jorgensen, J. Chandrasekhar, J. D. Madura, R. W. Impey, M. L. Klein, *J. Chem. Phys.* **1983**, *79*, 926.
[90] D. Beglov, B. Roux, *J. Chem. Phys.* **1994**, *100*, 9050.
[91] M. J. Frisch, G. W. Trucks, H. B. Schlegel, G. E. Scuseria, M. A. Robb, J. R. Cheeseman, G. Scalmani, V. Barone, G. A. Petersson, H. Nakatsuji, X. Li, M. Caricato, A. Marenich, J. Bloino, B. G. Janesko, R. Gomperts, B. Mennucci, H. P. Hratchian, J. V. Ortiz, A. F. Izmaylov, J. L. Sonnenberg, D. Williams-Young, F. Ding, F. Lipparini, F. Egidi, J. Goings, B. Peng, A. Petrone, T. Henderson, D. Ranasinghe, et al., *Gaussian09* **2013**.
[92] C. G. Mayne, J. Saam, K. Schulten, E. Tajkhorshid, J. C. Gumbart, *J. Comput. Chem.* **2013**, *34*, 2757.
[93] T. Darden, D. York, L. Pedersen, *J. Chem. Phys.* **1993**, *98*, 10089.

© 2021 Wiley-VCH GmbH